Nanoscale Advances

COMMUNICATION

View Article Online
View Journal | View Issue

Cite this: *Nanoscale Adv.*, 2019, **1**, 2167

Novel 3D hierarchically structured cauliflower-shaped SnO_2 nanospheres as effective photoelectrodes in hybrid photovoltaics†

Khalid Mahmood, ‡*[a] Muhammad Imran,‡[b] Madsar Hameed,[a] Faisal Rehman,[a] Syed Waqas Ahmad[a] and Faisal Nawaz[c]

Received 29th March 2019
Accepted 5th May 2019

DOI: 10.1039/c9na00192a

rsc.li/nanoscale-advances

Optical and electrical characteristics of wide bandgap metal oxides, namely the charge mobility, bandgap and energy level, directly define the performance and stability of photovoltaics. For the first time, novel three-dimensional (3D) hierarchically structured cauliflower-shaped SnO_2 nanospheres with nanorods on their surface were obtained by a simple hydrothermal method without any additives at low temperature. The obtained hierarchically structured SnO_2 nanospheres show large specific surface areas, proven to be efficient for sensitizer loading in both perovskite solar cells (PSCs) and dye-sensitized solar cells (DSSCs). The nanospheres could improve light harvesting and also enhance electron transport through the grain boundaries. Ultimately, a maximum power conversion efficiency of 10.37% is obtained for 3D hierarchically structured SnO_2 nanosphere-based DSSCs in which SnO_2 is used as the scattering layer, and a remarkable efficiency of 20.01% is achieved when 3D hierarchically structured SnO_2 nanospheres are employed as the electron transport material in PSCs. We trust that our work provides a new insight into construction and structural design of highly efficient hybrid photovoltaics.

1. Introduction

During the last several decades, wide bandgap metal oxides (MOs) have attracted great attention from the photovoltaic community owing to their outstanding electrical and optical characteristics as well as their excellent thermal and chemical stability in harsh environments.[1,2] On the basis of their distinct properties, wide bandgap MOs have been extensively applied in hybrid photovoltaics such as dye-sensitized solar cells (DSSCs) and perovskite solar cells (PSCs) in recent years.[3–9] Perovskite solar cells with excellent features such as high electron mobility, a long carrier lifetime, a high absorption coefficient, and an adjustable energy band gap have proven to be promising contenders for current photovoltaic technologies by attaining a remarkable power conversion efficiency (PCE) of 23.3%, the highest device efficiency reported to date.[10–14]

Wide bandgap MOs are usually employed in PSCs as an electron transporting layer (ETL), as they can harvest more light that can reach the perovskite absorber. MOs employed as an ETL in photovoltaics must have appropriate band alignment. The valence band maximum (VBM) and conduction band minimum (CBM) should be lower compared to those of the perovskite light absorber. Moreover, enhanced charge mobility is very crucial to transfer the carriers efficiently and retard the combination of charges within the ETL. Last but not least, the crystallinity of MOs boosts the device performance of PSCs.[15–22]

Among MOs, SnO_2 has been recently developed as an alternative ETL to widely used ZnO and TiO_2 in PSCs because of its wide bandgap, high electron mobility, low-temperature film formation, satisfactory band structure and chemical and photostability.[23–26] PSCs based on SnO_2 ETLs have demonstrated a remarkable development in terms of a high certified device efficiency of 20.9%, excellent photostability and a voltage exceeding 1.19 V.[27–29] These SnO_2 based ETLs have been synthesized mostly in the form of nanoparticles and nanosheets *via* different methods such as chemical bath deposition (CBD), atomic layer deposition (ALD) and electrospraying.[30–35] However, concerns about the additional improvement of device efficiency and stability are still unsolved for SnO_2-based ETLs produced by a facile method. It is therefore of great importance to develop a viable route such as a hydrothermal route to grow three-dimensional (3D) hierarchically structured SnO_2 ETLs in a simple way for device applications.

In this work, for the first time ever, we have exploited a low-temperature hydrothermal route to grow novel cauliflower

[a]*Department of Chemical & Polymer Engineering, University of Engineering & Technology Lahore, Faisalabad Campus, $3\frac{1}{2}$ km, Khurrianwala - Makkuana By-Pass, Faisalabad, Pakistan. E-mail: khalid@kaist.ac.kr*

[b]*Department of Chemical Engineering, Pakistan Institute of Engineering & Applied Sciences, Islamabad, Pakistan*

[c]*Department of Humanities & Basic Sciences, University of Engineering & Technology Lahore, Faisalabad Campus, $3\frac{1}{2}$ km. Khurrianwala - Makkuana By-Pass, Faisalabad, Pakistan*

† Electronic supplementary information (ESI) available. See DOI: 10.1039/c9na00192a

‡ Both authors contributed equally to this work.

shaped SnO_2 nanospheres without any additives. 3D hierarchically structured SnO_2 ETLs with a large surface area and enhanced electron transport were further synthesized by growing the nanorods on the surface of these cauliflower shaped SnO_2 nanospheres using a second hydrothermal step. The as-prepared SnO_2-based ETLs were further used in high efficiency and hysteresis-free perovskite solar cells. 3D hierarchically structured SnO_2 ETLs with an optimal thickness produce highly efficient mesoscopic PSCs with a maximum power conversion efficiency (PCE_{max}) of 20.01% compared to the cauliflower shaped SnO_2 nanospheres (16.98%). DSSCs with PCE_{max} of 10.37% were also fabricated using these novel 3D hierarchically structured SnO_2 films. These incredible device efficiencies were possible thanks to the growth of 3D hierarchically structured SnO_2 ETLs capable of fast electron transfer over long distances by reducing recombination losses.

2. Experimental section

2.1. Synthesis of cauliflower-shaped SnO_2 nanospheres

Cauliflower-shaped SnO_2 nanospheres were synthesized using a single-step hydrothermal method. In a typical synthesis procedure, 2 g of sodium stannate trihydrate ($Na_2SnO_3 \cdot 3H_2O$) and 0.5 g of sodium hydroxide pellets (NaOH) were dissolved in 80 mL distilled water. The solution was then transferred to a 100 mL Teflon-lined stainless steel autoclave for hydrothermal growth at 150 °C for 24 h. After that, the final product was thoroughly washed several times with ethanol and deionized water to remove the residual impurities. It was then dried at 100 °C for 2 h for further use.

2 g of the final powder (white in color) was then ground using a few drops of acetic acid and ethanol to dissolve the aggregates. The obtained solution was dispersed using an ultrasonicator and added to 2 mL terpineol as the dispersant and 1 g ethyl cellulose as the thickener in 15 mL ethanol. The resulting colloidal suspension was further concentrated by removing ethanol and the resultant paste was blade-coated onto fluorine-doped tin oxide (FTO) glass substrates and finally dried on a hot plate for 15 min at 120 °C.

2.2. Synthesis of 3D hierarchically structured SnO_2 nanospheres

The FTO substrates coated with cauliflower-shaped SnO_2 nanospheres obtained after the first hydrothermal step were further processed in a second hydrothermal cycle to grow the nanorods over their entire surface. The second hydrothermal cycle was carried out under the same experimental conditions (as described in Section 2.1) as used in the first hydrothermal step. The reaction temperature and time are the main factors for controlling the thickness of these films.

2.3. Electrode preparation and solar cell fabrication

The FTO substrates containing the SnO_2 films were then annealed at 450 °C for 1 h. After cooling, the substrates were then dipped in an ethanolic solution of ruthenium dye N719 for 20 h. Eventually, DSSCs were fabricated by placing a platinum counter electrode over the photoanode. A redox electrolyte solution was poured between the electrodes to complete the cell.

In case of PSCs, the ETLs were prepared by diluting the SnO_2 paste in ethanol and a monolayer of the SnO_2 nanostructures was spin-coated onto FTO glass substrates at 3000 rpm for 15 s followed by sintering at 450 °C for 1 h. The solution of perovskites $(FAPbI_3)_{0.85}(MAPbBr_3)_{0.15}$ was made by dissolving 344 mg of $NH_2CH{=}NH_2I$ (1.0 M), 44.8 mg CH_3NH_3Br (0.2 M) fine powders with 146.8 mg $PbBr_2$ (0.2 M) and 1014 mg PbI_2 (1.1 M) into a mixture of solvents DMSO and DMF (1 : 4, v/v). The as-prepared perovskite solution was then spin-coated onto the SnO_2 nanostructures at 3000 rpm for 40 s, and additionally 80 μL of chloroform was dropped during the last 10 s followed by annealing at 130 °C for 20 min. The hole transporting material of the spiro-OMeTAD solution was spin-coated over the perovskite layer at 2500 rpm for 30 s. Finally, gold electrodes were deposited on the top of the cells with a thickness of about 65 nm. The complete device architecture of PSCs used in this work is shown in Scheme S1.†

2.4. Characterization

The morphology of the SnO_2 nanostructures was obtained using a field-emission scanning electron microscope (FE-SEM, SU8010, Hitachi). Current–voltage (J–V) curves of the devices were measured with the help of a Keithley 2400 source meter by adjusting the light intensity to 100 mW cm^{-2} *via* a calibrated silicon solar cell. The devices were stored in the dark where the relative humidity was around 20–25%. A photoluminescence (PL) test was performed *via* a spectrofluorometer. The electron lifetime was obtained with the help of a transient photocurrent–voltage spectroscopy system. Transmittance and absorbance spectra of the nanostructures were collected on an ultraviolet-visible (UV-Vis) spectrophotometer.

3. Results and discussion

In Fig. 1b, the surface FESEM image of SnO_2 nanospheres under low magnification shows that the nanostructures were spherical with a diameter of 250–300 nm. The surface FESEM image under high magnification in Fig. 1a shows pyramidal crystal facets. They were uniformly formed on the surface with an average length of 70–100 nm. The interior of these nanospheres (Fig. 1b) is in fact composed of densely packed nanorods. These novel SnO_2 nanospheres have the shape of a cauliflower where the nanorod bundles are smaller and more distinct. This facile single-step hydrothermal method is highly suitable for the large scale synthesis of monodisperse cauliflower-shaped SnO_2 nanospheres with narrow size distribution. The cauliflower-shaped SnO_2 nanospheres were further subjected to a hydrothermal step in order to produce 3D hierarchical SnO_2 nanostructures with nanorods on their surfaces as well. In Fig. 1c, we exhibit the FESEM image of the 3D hierarchical SnO_2 nanostructures which show a novel nanoflower like morphology having a bunch of nanorods. The high resolution FESEM image in Fig. 1d clearly shows that these nanorods contain additional

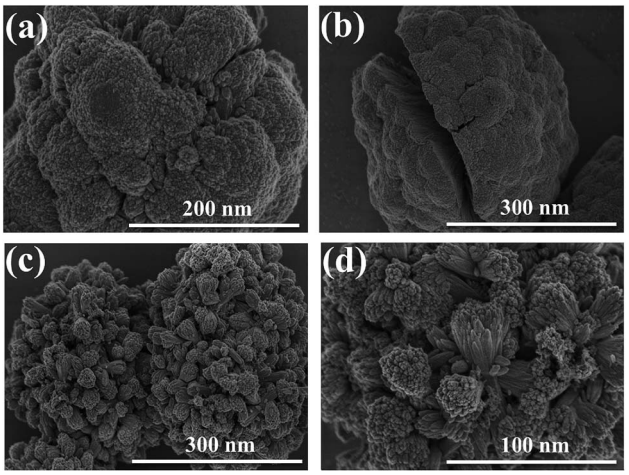

Fig. 1 Plane-view FESEM images of cauliflower-shaped SnO_2 nanospheres at (a) high resolution and (b) low resolution showing that the inside of each cauliflower is made of tiny nanorods and surface FESEM images of 3D hierarchical SnO_2 nanostructures at (c) low resolution and (d) high resolution exhibiting that nanorods are grown over the entire surface of the nanosphere, respectively.

bunches of aligned nanorods. These types of 3D hierarchical SnO_2 nanostructures have several crucial benefits, such as a large surface area and improved perovskite light-absorber filling, superior light scattering ability and faster charge extraction capabilities than the cauliflower-shaped SnO_2 nanospheres. These novel 3D hierarchical SnO_2 nanospheres with a cauliflower-shape are reported for the first time. The side-view SEM image of the 3D hierarchical SnO_2 nanospheres is displayed in Fig. S1.† It can be seen clearly that the 3D hierarchical SnO_2 nanospheres are completely covering the entire cross-section of the FTO glass substrate. The optical transmittance spectra of the cauliflower-shaped SnO_2 nanospheres and 3D hierarchical SnO_2 films are exhibited in Fig. S2.† Both types of nanostructures exhibited high optical transmittance in the UV-vis range while a slight reduction in transmissivity is seen for the cauliflower-shaped SnO_2 nanospheres compared to the 3D hierarchical SnO_2 films. Furthermore, in Fig. S3† we show the absorbance spectra of the corresponding nanostructures. 3D hierarchical SnO_2 films exhibited improved absorbance in the UV-Vis range proving that this type of nanostructure scatters more light than the cauliflower-shaped SnO_2 nanospheres.

Using these SnO_2 nanostructures with sufficiently increased thicknesses, we have assembled both PSC and DSSC devices, respectively. The representative *J–V* curves (both in the forward and reverse scan) of the PSCs based on two distinct SnO_2 nanostructures are displayed in Fig. 2a, and the parameters are summarized in Table 1. PSCs based on ETLs with cauliflower-shaped SnO_2 nanospheres showed an average power conversion efficiency (PCE_{avg}) of 15.05%, with a short-circuit current-density (J_{SC}) of 20.3 mA cm^{-2}, an open-circuit voltage (V_{OC}) of 1030 mV, and a fill factor (FF) of 72%. With the employment of ETLs based on 3D hierarchical SnO_2 nanospheres, PSCs demonstrated a significantly enhanced device performance (with a PCE_{avg} of 17.03%) and mainly inhibited hysteresis

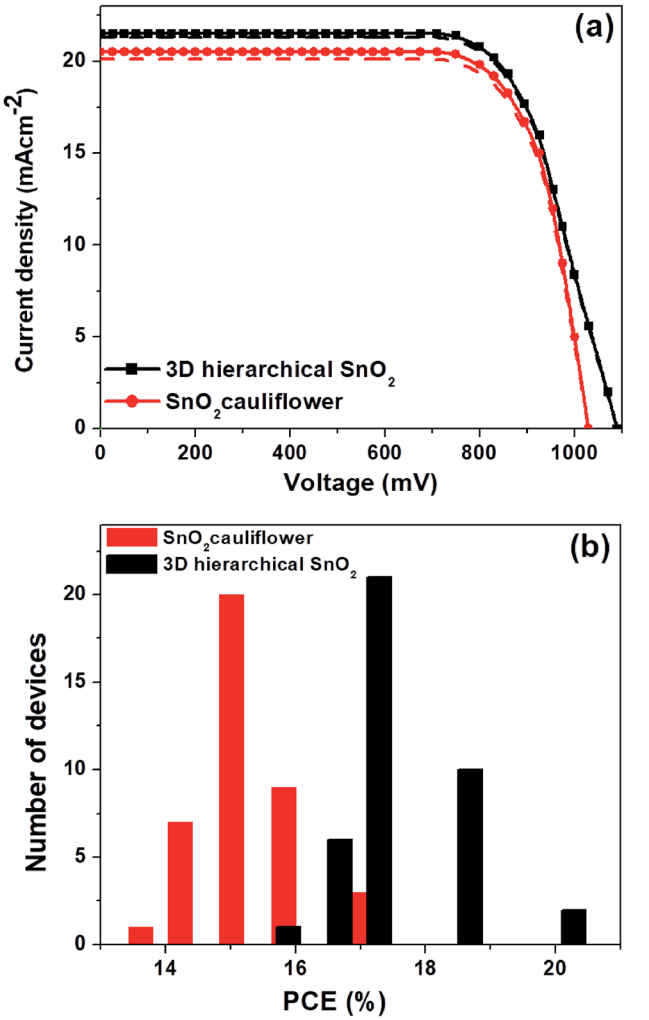

Fig. 2 (a) Comparison of *J–V* curves of PSCs based on two distinct SnO_2 nanostructures and (b) histograms of the corresponding PSCs showing variations in the PCE for 45 individual cells for each nanostructure.

behavior. The improved device performance of 3D hierarchical SnO_2 nanospheres ETLs is due to their improved light-harvesting ability, complete pore filling, fast charge transport and reduced charge recombination. The hysteresis-free behavior is credited to the enhanced charge collection and transport at the SnO_2/perovskite light-absorber interface. Optimization was checked systematically together with device reproducibility which was confirmed *via* statistical distribution of the device performance. Fig. 2b shows the histogram of the PCE measured for 45 individual devices with two distinct SnO_2 nanostructures. These devices show a high degree of reproducibility in the PCE. As observed in Fig. 2b, the statistical analysis show that almost all devices based on 3D hierarchical SnO_2 nanospheres have a higher PCE compared to the devices based on cauliflower-shaped SnO_2 nanospheres. The average PCE of the devices with 3D hierarchical SnO_2 nanosphere and cauliflower-shaped SnO_2 nanosphere ETLs is 17.03% and 15.05%, respectively.

Table 1 Device parameters obtained in different scanning directions for two distinct SnO_2 nanostructure based ETLs

ETL	Scan direction	J_{SC} (mA cm^{-2})	V_{OC} (mV)	FF (%)	PCE_{avg} (%)	PCE_{max} (%)
SnO_2 cauliflower	Reverse	20.5	1030	72	15.20 ± 0.10	17.10
	Forward	20.1	1030	72	14.90 ± 0.10	16.86
	Average	20.3	1030	72	15.05 ± 0.10	16.98
3D hierarchical SnO_2	Reverse	21.5	1090	73	17.10 ± 0.12	20.01
	Forward	21.3	1090	73	16.94 ± 0.11	19.83
	Average	21.4	1090	73	17.03 ± 0.12	19.92

The thickness of ETLs plays a crucial part in defining the photovoltaic performance, which is optimized by properly tuning the experimental conditions in this work. The typical *J–V* curves of PSCs with two distinct SnO_2 nanostructures with varying film thicknesses are shown in Fig. 3. The cells achieved the best performance with the thinnest ETLs (~435 nm, in Fig. 2a). Further increase of the ETL thickness (Fig. 3) deteriorated the device performance due to poor perovskite loading into the ETLs and slow charge transport in thicker films.

In Fig. 4a, we show the *J–V* curve (reverse scan) of the best performing PSC with 3D hierarchical SnO_2 nanospheres. More specifically, the champion device showed the highest PCE of 20.01% with a V_{OC}, J_{SC}, and FF of 1155 mV, 22.8 mA cm^{-2}, and 76%, respectively. This remarkable device efficiency of 20.01% is among the best results for PSCs with 3D hierarchical SnO_2 nanospheres and is reported for the first time ever, to the best of our knowledge. In order to further confirm the reliability of the PSCs produced in this study, the steady state efficiencies of the 3D hierarchical SnO_2 nanosphere based devices are also studied. As exhibited in Fig. 4b, the device showed a stable J_{SC} of 22.8 mA cm^{-2} and a PCE of 20.01% at a voltage bias of 0.83 V, which is possibly initiated by the faster charge transfer and suppressed charge recombination due to the improved contact interface between the perovskite and 3D hierarchical SnO_2 nanosphere based ETL. The hysteresis behavior of the best performing PSCs was also tested by collecting the *J–V* curves

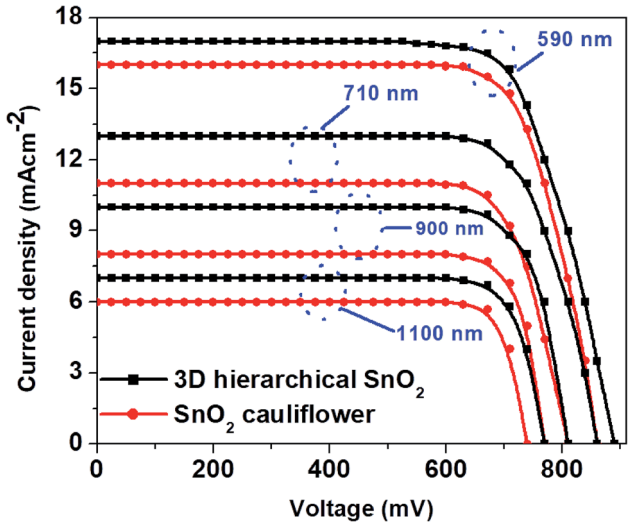

Fig. 3 *J–V* curves as a function of the ETL thickness for two distinct SnO_2 nanostructures.

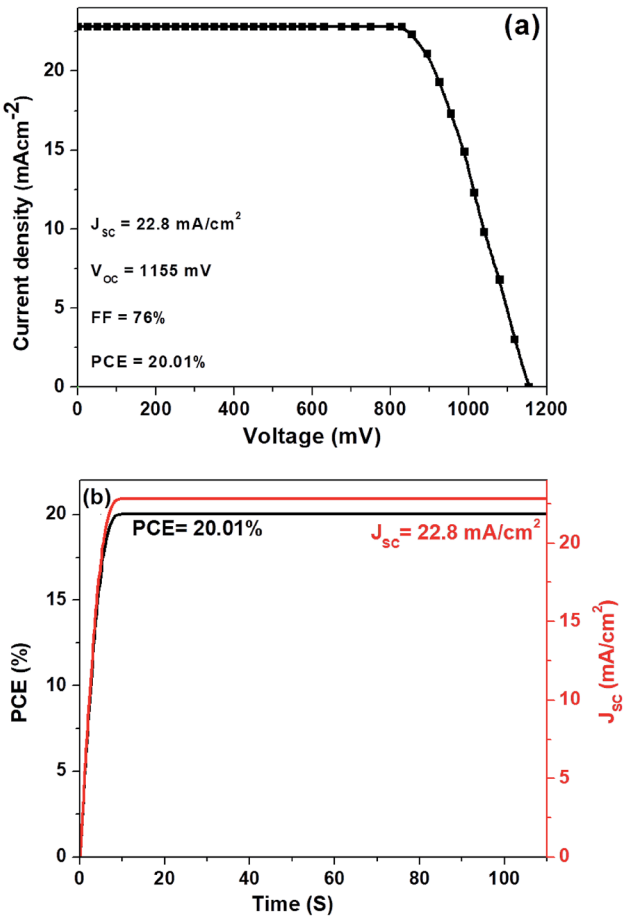

Fig. 4 (a) *J–V* plot (reverse scan) for the best performing PSCs with 3D hierarchical SnO_2 nanospheres and (b) the steady state efficiency of the corresponding devices measured at maximum power output.

both in the forward and reverse directions as seen in Fig. 5. Negligible hysteresis is observed for these devices, thanks to the improved charge passivation and transfer at the SnO_2 ETL/perovskite light-absorber interface.

For comparison and application in DSSCs, SnO_2 nanostructures with a thickness of around 8 μm were used. Fig. 6 shows the *J–V* plots of the DSSCs based on these two distinct photoanode films. Among these two photoanodes, the DSSCs fabricated with 3D hierarchical SnO_2 nanospheres demonstrate a higher J_{SC} due to a large amount of dye adsorption. The dye loading amount of 3D hierarchical SnO_2 nanospheres was 18.56 × 10^{-8} mol cm^{-2} which was much higher than that of the

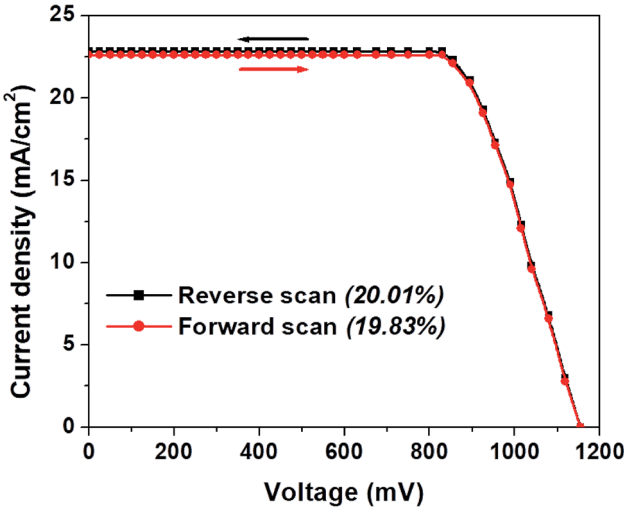

Fig. 5 J–V plot (both in reverse and forward scans) for the best performing PSCs with 3D hierarchical SnO_2 nanospheres showing their hysteresis-free behavior.

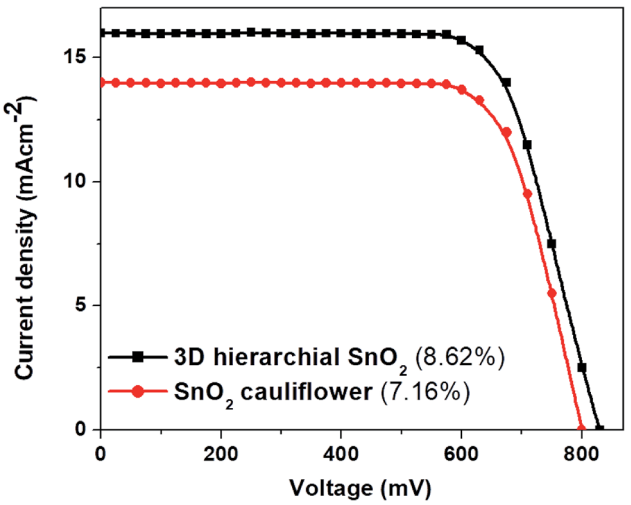

Fig. 6 Comparison of J–V curves of DSSCs fabricated with two distinct SnO_2 nanostructures.

cauliflower-shaped SnO_2 nanospheres (8.71×10^{-8} mol cm^{-2}). Since the J_{SC} depends strongly on both light utilization and absorption, multiple scattering produced by the 3D hierarchical SnO_2 nanospheres would enhance the paths of the incident light within the photoanode film, and thus improve the chances of dye molecules to be excited more. The V_{OC} of 3D hierarchical SnO_2 nanosphere-based DSSCs is relatively higher than that of the ones with cauliflower-shaped SnO_2 nanospheres, thanks to the well interconnected structure preventing charge recombination with I_3^- in the electrolyte. In addition, DSSCs with 3D hierarchical SnO_2 nanospheres demonstrate an improved PCE of 8.62%, which is assigned to the high dye loading and proper light confinement within the photoanode film. It is worth mentioning that the best efficiency of 10.37% (in Fig. 7) of DSSCs based on 3D hierarchical SnO_2 nanospheres ranks at the top of the efficiencies of SnO_2-based DSSCs reported to date.

In Fig. 7, we show the J–V plots of the best performing PSCs and DSSCs based on 3D hierarchical SnO_2 nanosphere films. The DSSC attained a remarkable PCE_{max} of 10.37% with a J_{SC} of 18 mA cm^{-2}, a FF of 67% and a V_{OC} of 860 mV. The perovskite device showed a remarkably superior efficiency, demonstrating a PCE_{max} of 20.01%, the highest and never been reported value to date. These new findings clearly prove that, as novel nanostructures, 3D hierarchical SnO_2 nanosphere films must be superior building blocks for hybrid photovoltaics to obtain better device performances than conventional SnO_2 nanoparticle based films which have been extensively used in both solar energy applications and other research areas.

We also show the steady-state PL spectra (Fig. 8a) of perovskites based on different nanostructures of SnO_2 to explain the reason behind the fast charge extraction capabilities of 3D hierarchical SnO_2 nanostructures compared to the cauliflower-shaped SnO_2 nanospheres. The perovskites formed on 3D hierarchical SnO_2 nanostructures exhibit a less intense PL peak compared to cauliflower-shaped SnO_2 nanospheres, which enhances electron transfer from the perovskites to the oxide layer. Moreover, an intensity-modulated photovoltage spectroscopy (IMVS) test was also performed (Fig. 8b) to evaluate the electron lifetime of perovskites deposited on different SnO_2 nanostructures. A longer electron lifetime was seen for the perovskites based on 3D hierarchical SnO_2 nanostructures compared to the cauliflower-shaped SnO_2 nanospheres, demonstrating reduced charge recombination.

The stability of the performance of PSCs was also studied constantly in dry air. The cells based on 3D hierarchical SnO_2 nanostructures showed superior long-term stability even after 100 days (Fig. S4†) compared to the cells based on cauliflower-shaped SnO_2 nanospheres. The improved shelf stability of SnO_2 based PSCs can be assigned to the robust nature of SnO_2 against moisture and oxygen. In addition, the highly porous nature of the SnO_2 nanostructures facilitates better pore filling

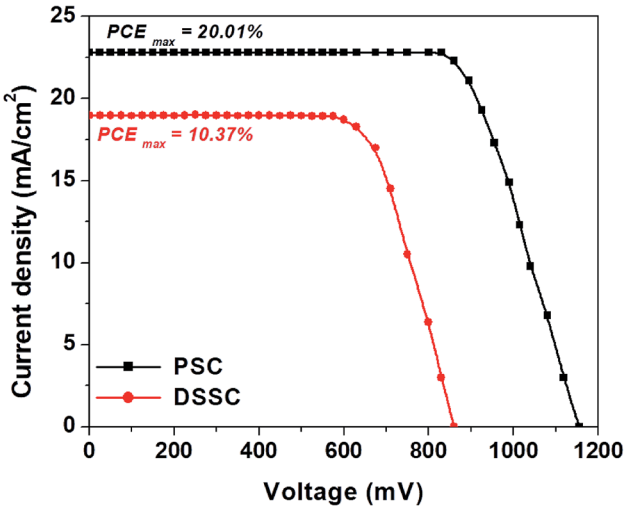

Fig. 7 Comparison of J–V curves of best performing devices of both PSCs and DSSCs based on the 3D hierarchical SnO_2 nanosphere ETL.

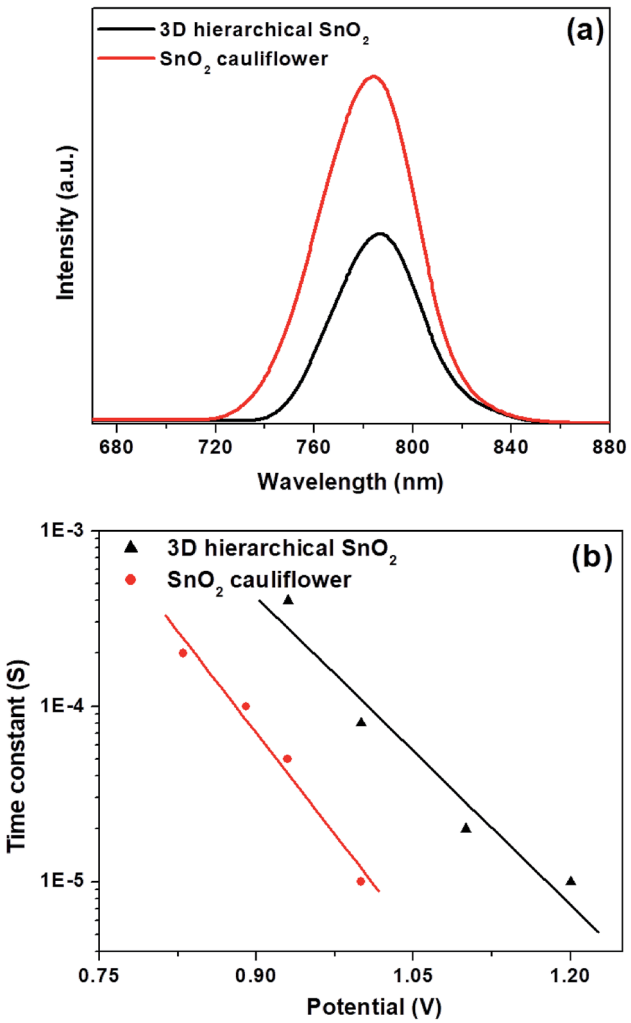

Fig. 8 (a) Steady-state PL spectra of perovskites on different SnO_2 nanostructures and (b) electron lifetime for the perovskites based on different SnO_2 nanostructures.

and the formation of a better interface between the perovskite and the ETL which prevents perovskite phase separation. Thus an extended lifetime was seen for the devices constructed using SnO_2 nanostructures.

4. Conclusion

To summarize, SnO_2 ETLs based on novel 3D hierarchical SnO_2 nanospheres have been prepared using a facile hydrothermal route for the first time ever. These ETLs not only have a large surface area, but also fast charge transport, improved light-harvesting ability and inhibited charge recombination, which are recognized through the remarkable improvement in terms of the device efficiency in both perovskite and dye sensitized solar cells. Perovskite devices were made by using a nanometer size film of 3D hierarchical SnO_2 nanospheres to produce a high PCE of 20.01%. DSSCs were assembled using thicker photoanodes, demonstrating the best PCE of 10.37%, the highest ever value obtained using hierarchical SnO_2 photoelectrodes. These findings obviously prove that 3D hierarchical SnO_2 nanospheres have huge potential for building next generation mesoscopic photovoltaics. Additionally, these novel wide bandgap metal oxide films are anticipated to also exhibit great potential in the fields of electromagnetism, lithium batteries and sensors.

Conflicts of interest

There are no conflicts to declare.

Acknowledgements

The authors gratefully acknowledge the financial support from the Higher Education Commission (HEC) of Pakistan.

References

1 J. Lee, M. C. Orilall, S. C. Warren, M. Kamperman, F. J. DiSalvo and U. Wiesner, *Nat. Mater.*, 2008, **7**, 222.
2 H. J. Bolink, E. Coronado, J. Orozco and M. Sessolo, *Adv. Mater.*, 2009, **21**, 79–82.
3 M. F. M. Noh, C. H. Teh, R. Daik, E. L. Lim, C. C. Yap, M. A. Ibrahim, N. A. Ludin, A. R. bin Mohd Yusoff, J. Jang and M. A. M. Teridi, *J. Mater. Chem. C*, 2018, **6**, 682–712.
4 Q. Jiang, X. Zhang and J. You, *Small*, 2018, **14**, 1801154.
5 P. Zhang, J. Wu, T. Zhang, Y. Wang, D. Liu, H. Chen, L. Ji, C. Liu, W. Ahmad and Z. D. Chen, *Adv. Mater.*, 2018, **30**, 1703737.
6 K. Mahmood, S. Sarwar and M. T. Mehran, *RSC Adv.*, 2017, **7**, 17044–17062.
7 K. Mahmood, B. S. Swain and A. Amassian, *Adv. Mater.*, 2015, **27**, 2859–2865.
8 K. Mahmood and H. J. Sung, *J. Mater. Chem. A*, 2014, **2**, 5408.
9 K. Mahmood, A. Khalid and M. T. Mehran, *Sol. Energy*, 2018, **173**, 496–503.
10 N. J. Jeon, J. H. Noh, Y. C. Kim, W. S. Yang, S. Ryu and S. I. Seok, *Nat. Mater.*, 2014, **13**, 897.
11 N. J. Jeon, J. H. Noh, W. S. Yang, Y. C. Kim, S. Ryu, J. Seo and S. I. Seok, *Nature*, 2015, **517**, 476.
12 W. S. Yang, B.-W. Park, E. H. Jung, N. J. Jeon, Y. C. Kim, D. U. Lee, S. S. Shin, J. Seo, E. K. Kim and J. H. Noh, *Science*, 2017, **356**, 1376–1379.
13 N. J. Jeon, H. Na, E. H. Jung, T.-Y. Yang, Y. G. Lee, G. Kim, H.-W. Shin, S. I. Seok, J. Lee and J. Seo, *Nat. Energy*, 2018, **3**, 682.
14 Energy Laboratory (NREL), *Best Research-Cell Efficiencies Chart*, see https://www.nrel.gov/pv/assets/pdfs/pv-efficiencies-07-17-2018.pdf for National Renewable, accessed September 2018.
15 K. Mahmood, A. Khalid and M. T. Mehran, *Sol. Energy*, 2018, **173**, 496–503.
16 K. Mahmood, M. T. Mehran, F. Rehman, M. S. Zafar, S. W. Ahmad and R. K. Song, *ACS Omega*, 2018, **3**, 9648–9657.
17 K. Mahmood, A. Khalid, M. S. Zafar, F. Rehman, M. Hameed and M. T. Mehran, *J. Colloid Interface Sci.*, 2019, **538**, 426–432.

18 K. Mahmood, M. Hameed, F. Rehman, A. Khalid, M. Imran and M. T. Mehran, *Appl. Phys. A*, 2019, **125**, 83.
19 S. Li, P. Zhang, H. Chen, Y. Wang, D. Liu, J. Wu, H. Sarvari and Z. D. Chen, *J. Power Sources*, 2017, **342**, 990–997.
20 T. Zhang, F. Wang, P. Zhang, Y. Wang, H. Chen, J. Li, J. Wu, L. Chen, Z. D. Chen and S. Li, *Nanoscale*, 2019, **11**, 2871–2877.
21 W. Ahmad, D. Liu, W. Ahmad, Y. Wang, P. Zhang, T. Zhang, H. Zheng, Z. D. Chen and S. Li, *IEEE Journal of Photovoltaics*, 2019, **9**, 200–206.
22 T. Zhang, J. Wu, P. Zhang, W. Ahmad, Y. Wang, M. Alqahtani, H. Chen, C. Gao, Z. D. Chen, Z. Wang and S. Li, *Adv. Opt. Mater.*, 2018, **6**, 1701341.
23 Y. Bai, Y. Fang, Y. Deng, Q. Wang, J. Zhao, X. Zheng, Y. Zhang and J. Huang, *ChemSusChem*, 2016, **9**, 2686.
24 S. S. Mali, J. V. Patil, H. Kim and C. K. Hong, *Nanoscale*, 2018, **10**, 8275.
25 Q. Liu, M.-C. Qin, W.-J. Ke, X.-L. Zheng, Z. Chen, P.-L. Qin, L.-B. Xiong, H.-W. Lei, J.-W. Wan, J. Wen, G. Yang, J.-J. Ma, Z.-Y. Zhang and G.-J. Fang, *Adv. Funct. Mater.*, 2016, **26**, 6069.
26 S. Kumar and A. Dhar, *ACS Appl. Mater. Interfaces*, 2016, **8**, 18309–18320.
27 Q. Jiang, Z. Chu, P. Wang, X. Yang, H. Liu, Y. Wang, Z. Yin, J. Wu, X. Zhang and J. You, *Adv. Mater.*, 2017, **29**, 1703852.
28 H. Tao, Z. B. Ma, G. Yang, H. N. Wang, H. Long, H. Y. Zhao, P. L. Qin and G. J. Fang, *Appl. Surf. Sci.*, 2018, **434**, 1336–1343.
29 P. Zhou, J. Wu, Y. Tu, M. Zhen, J. Huo, Y. Wei and Z. Lan, *Sol. Energy*, 2016, **137**, 579–584.
30 C. L. Wang, D. W. Zhao, C. R. Grice, W. Q. Liao, Y. Yu, A. Cimaroli, N. Shrestha, P. J. Roland, J. Chen, Z. H. Yu, P. Liu, N. Cheng, R. J. Ellingson, X. Z. Zhao and Y. F. Yan, *J. Mater. Chem. A*, 2016, **4**, 12080–12087.
31 D. Pérez-del-Rey, P. P. Boix, M. Sessolo, A. Hadipour and H. J. Bolink, *J. Phys. Chem. Lett.*, 2018, **9**, 1041–1046.
32 K. Mahmood, A. Khalid, F. Nawaz and M. T. Mehran, *J. Colloid Interface Sci.*, 2018, **532**, 387–394.
33 Y. Lv, P. Wang, B. Cai, Q. Ma, X. Zheng, Y. Wu, Q. Jiang, J. Liu and W. -H. Zhang, *Sol. RRL*, 2018, **2**, 1800133.
34 Y. Chen, Z. Yang, S. Wang, X. Zheng, Y. Wu, N. Yuan, W. -H. Zhang and S. Liu, *Adv. Mater.*, 2018, **30**, 1805660.
35 Y. Wu, P. Wang, S. Wang, Z. Wang, B. Cai, X. Zheng, Y. Chen, N. Yuan, J. Ding and W. -H. Zhang, *ChemSusChem*, 2018, **11**, 837.